



## ISTITUTO NAZIONALE DI RICERCA METROLOGICA Repository Istituzionale

### A Novel Sensor-Integrated Aperture Coupled Microwave Patch Resonator for Humidity Detection

This is the author's accepted version of the contribution published as:

*Original*

A Novel Sensor-Integrated Aperture Coupled Microwave Patch Resonator for Humidity Detection / Gugliandolo, Giovanni; Naishadham, Krishna; Neri, Giovanni; Fernicola, Vito; Donato, Nicola. - In: IEEE TRANSACTIONS ON INSTRUMENTATION AND MEASUREMENT. - ISSN 0018-9456. - (2021), p. art. 9506611. [10.1109/TIM.2021.3062191]

*Availability:*

This version is available at: 11696/68476 since: 2021-05-28T12:40:48Z

*Publisher:*

IEEE

*Published*

DOI:10.1109/TIM.2021.3062191

*Terms of use:*

This article is made available under terms and conditions as specified in the corresponding bibliographic description in the repository

*Publisher copyright*

IEEE

© 20XX IEEE. Personal use of this material is permitted. Permission from IEEE must be obtained for all other uses, in any current or future media, including reprinting/republishing this material for advertising or promotional purposes, creating new collective works, for resale or redistribution to servers or lists, or reuse of any copyrighted component of this work in other works

(Article begins on next page)

# A Novel Sensor-Integrated Aperture Coupled Microwave Patch Resonator for Humidity Detection

Giovanni Gugliandolo, *Member, IEEE*, Krishna Naishadham, *Senior Member, IEEE*, Giovanni Neri, Vito Fericola and Nicola Donato, *Senior Member, IEEE*

**Abstract**—Wireless sensor elements integrated with miniaturized antennas are useful in various applications such as wearable chemical and environmental sensors and IoT sensor nodes. A major problem in antenna operation is detuning of the antenna bandwidth due to loading by the sensor element. In this paper, we report on the integration of an interdigitated capacitor (IDC), acting as a sensor, into an Aperture Coupled Patch (ACP) antenna, such that weak coupling is established between the IDC and the rectangular patch resonator. Because of low mutual coupling, during the sensing process the antenna is not detuned out of its operational bandwidth and its performance is not compromised by the presence of the sensor and vice versa. A sensing material (barium titanate film) is deposited on the IDC located at the edge of the microstrip line used to slot-feed the ACP antenna. A change in the material permittivity is transduced into a variation of resonant frequency of the antenna. We describe the design and fabrication of the IDC sensor-integrated ACP antenna, and demonstrate the measured sensing performance at different temperatures and relative humidity concentrations.

**Index Terms**—patch antenna, gas sensor, microwave resonator, humidity sensor, internet-of-things, wireless sensor.

## I. INTRODUCTION

THE global sensors market is increasing every year. According to Allied Market Research (AMR), it will grow at an annual rate of 11.3% until 2022, when the market will reach \$241 billion [1]. A key role in this scenario is played by the Internet-of-Things (IoT) and mobile technologies. Nowadays, sensors are integrated in many objects of our everyday life, for example, fitness and wellness sensors (like Fitbit), proximity sensors and accelerometers in the cell phone, indoor air quality monitors, etc. Novel sensors for many applications, including environmental monitoring, healthcare and industrial processes, are being developed using metal oxide semiconductors, electrochemical and nanotechnologies [2]-[12].

Recently, there has been significant interest in microwave

resonator or antenna-based sensors, which utilize change in resonant frequency or dielectric constant as a marker for gas detection [13]-[25]. These low-power and relatively low-cost sensors, capable of operation at ambient temperature, can be readily integrated in a Wireless Sensor Network (WSN) by interfacing the antenna for each node with the corresponding sensor, the signal conditioning, control and communications circuitry. The difference between a resonator-type sensor and an antenna-type sensor is simply that the former is not designed with the additional functionality of radiation of electromagnetic (EM) waves in mind, which is necessary for operation as a wireless node. The latter encompasses both functions in a compact node and obviates the need for a separate antenna. A microwave sensor for gas detection is generally characterized by a planar resonator structure such as a patch or a slot covered in whole or partially by the sensing material, as thin or thick film. When the gas target is adsorbed on the surface of the sensing film, the permittivity or the impedance of the surface changes. This process is responsible for variation in the resonant frequency as well as the quality factor of the resonator, because the surface impedance of the sensor film loads the resonator and perturbs its resonance. It is not only the resonant frequency, but the amplitude and phase of the detected signal at resonance are also affected by such loading. Thus, in principle, microwave sensors offer multivariate signal processing capability to reduce the influence of confounding effects (such as cross-sensitivity to analytes of similar chemical nature as the one being detected).

For an antenna-based sensor node, the first step is to couple the sensor with an antenna, generally on the same board as the processing electronics and the sensor element. The extent of coupling between the sensor and the antenna will affect the node performance (i.e. sensing properties, antenna radiation pattern, power gain, etc.). The integration of sensors in antennas is widely described in literature (cf. [26]). Novel antenna configurations with carbon nanotube (CNT) loading of a microstrip patch or a dipole resonator have been explored for

G. Gugliandolo is with the MIFT Department, University of Messina, 98158 Messina, Italy (e-mail: giovanni.gugliandolo@unime.it).

K. Naishadham, is with the School of Electrical Engineering Georgia Institute of Technology, Atlanta, GA 30332, USA (e-mail: krishna.n@ieee.org).

G. Neri and N. Donato are with the Department of Engineering, University of Messina, Contrada di Dio, S. Agata, 98158 Messina, Italy (e-mails: gneri@unime.it, ndonato@unime.it).

V. Fericola is with the Istituto Nazionale di Ricerca Metrologica (INRiM), Strada delle Cacce, 10135 Torino, Italy (e-mail: v.fericola@inrim.it).

gas detection using either the return loss [17] or the resonant frequency shift [18]-[20] as the detection marker. The selective carbon loading over a small gap in a tuning stub connected to the radiating edge of a microstrip patch (6 GHz center frequency) reduced the radiation efficiency from 99% (without the CNT film) to about 50% (with the film) and resulted in a frequency shift between 100 to 300 MHz, thereby detuning the antenna bandwidth and compromising its performance [18], [19]. In contrast, Chopra et al. [13] discuss the design of a circular patch resonator at 3.9 GHz, completely coated with a mixture of CNT powder and a conductive epoxy, for ammonia detection. Exposure of the CNT mixture to ammonia changes effective permittivity of the patch and shifts its resonant frequency. The large area of carbon loading increases the resonator losses and deteriorates the quality factor. Thus, the antenna efficiency was less than 10%, and even with a high ammonia concentration (1000 ppm), only 5 MHz shift was detected in a controlled gas flow chamber. *Therefore, the shape and location of the sensor element should be designed such that there is weak coupling between the antenna and the sensor and the antenna losses are minimal.*

This paper presents a novel design approach to weakly couple the antenna and the sensor film, involving the integration of an interdigitated capacitor (IDC) along the electromagnetically coupled microstrip feed line of an aperture coupled patch (ACP) antenna. Nano-powder of barium titanate with urea coating ( $\text{BaTiO}(\text{C}_2\text{O}_4)_2/\text{CO}(\text{NH}_2)_2$ ) is deposited as the sensor material between the interdigitated electrodes to detect humidity. For convenience, the IDC may be alternatively referred henceforth as the sensor or the sensing element. The innovation in this design is that the antenna characteristics are not influenced by the presence of the sensor and vice versa, as demonstrated in the sequel below. In particular, the loading by the IDC and the activated sensor film (in a detection event) produces a distinct measurable frequency shift without detuning the antenna bandwidth. We investigate the performance of this Sensor-integrated Aperture Coupled Patch (SACP) antenna as a humidity sensor, and demonstrate measured sensing performance at different temperatures and relative humidity levels.

The paper is organized as follows. In Section II, the design and fabrication of the SACP antenna are reported. In Section III, baseline measurements of the ACP antenna are described, and the antenna response (without the sensor film) to humidity and temperature variation is investigated. In Section IV, the sensing material synthesis and its deposition over the IDC are described. Finally, Section V presents and discusses the sensing properties of the SACP antenna at different temperatures and relative humidity concentrations. Section VI summarizes the conclusions.

## II. SENSOR INTEGRATED ANTENNA DESIGN

The ACP antenna, introduced by Pozar in [27], [28], comprises of the patch radiator on one substrate, electromagnetically coupled to a microstrip feedline placed on another substrate, through a narrow slot aperture in the ground plane that separates the two substrates (Fig. 1). This

configuration enables reduction of the EM interference between the feed network and the main radiator, and minimizes the feed radiation. Moreover, direct connections between the feed and the antenna element are avoided, mitigating the parasitic inductance and capacitance of alternate feeding mechanisms, such as coaxial probe feed and microstrip line feed, respectively.

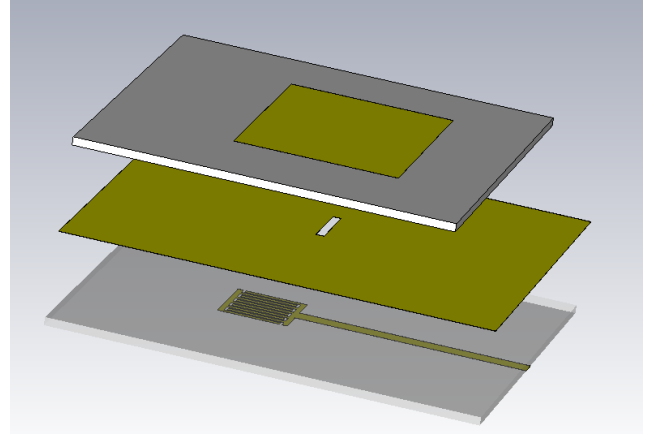


Fig. 1. Aperture coupled patch antenna geometry (3D exploded view). The top layer is the antenna substrate with a rectangular patch antenna shown, the middle layer is the ground plane with a centered slot parallel to the patch width, and the bottom layer is the microstrip feed substrate hosting a transmission line terminated by an IDC upon which the sensor film is deposited.

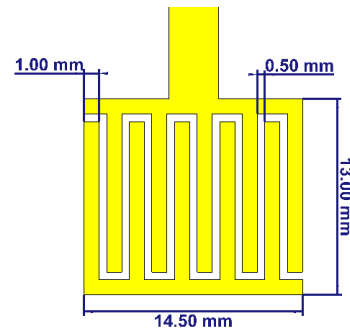


Fig. 2. Geometry of the IDC integrated into the ACP antenna.

The ACP antenna has been researched and reviewed in literature for EM applications such as phased arrays and radar [29]-[32]. However, its integration with a sensor for potential application as a wireless node has never been addressed. Interdigitated electrodes offer large surface area to enhance the transduced signal arising from a chemical reaction between the sensor film and the analyte being detected, thus improving the sensitivity. An interdigitated capacitor was first deployed as a sensor in a printed antenna structure in [33], [34] wherein coupling between the two dominant modes on an annular slot antenna was adjusted to widen the bandwidth by controlling the capacitance along the microstrip feed line. The IDC enables change in input impedance and bandwidth of the antenna which can be used as markers in the detection signal. In this paper, an IDC sensing element is integrated into an ACP antenna for the first time and its performance as a humidity sensor is investigated. Preliminary design of an IDC coated with barium

titanate-based sensing material, which forms the basis for sensor integration with the ACP antenna, has been presented in the conference proceeding [35]. This article is an extended version of this work. The sensing material was deposited between the IDC electrodes by drop-coating in a specially made 2-port IDC gas testing fixture, and its baseline performance without gas exposure has been established. Building on the sensor baseline characterization in [35], in this paper, we investigate the integration of the IDC sensor element along the feed line of the ACP antenna. The SACP design for a humidity sensor is described in detail, and the sensor fabrication, materials synthesis and physical properties are addressed. Microwave measurements are performed to validate the design and evaluate the sensing performance at various humidity levels and temperatures.

As depicted in Fig. 1, an IDC is introduced as a sensing element in the proximity-coupled microstrip feed line of an ACP antenna. The geometry of the IDC is sketched in Fig. 2. One end of the IDC is connected to the feed line and the other end is left open-circuited. A short circuit may be used instead, but the short introduces additional inductance and complicates the impedance matching at the antenna input. Through simulations, we optimize the IDC dimensions and its placement along the line so that without any nanomaterial loading, the antenna presents a distinct resonance at 2.45 GHz, the center frequency of the ISM band. Due to its weak coupling, the antenna resonant frequency and return loss will not be compromised after the sensing material deposition and the detection process, as will be shown by the measurements in Section IV.

The rectangular patch is first designed using the classic formulas reported in literature (cf. [36]). Its length ( $L = 40$  mm) and width ( $W = 30$  mm) are calculated for 2.45 GHz resonance using Rogers RO4003C substrate with thickness  $h = 1.52$  mm and dielectric constant [35]. The substrate has the dimensions  $80 \times 75$  mm. The feedline on the second substrate is designed for an input impedance of 50 ohms. In standard ACP design, the feed line is terminated in a quarter wavelength stub. The capacitance of the open end of the stub compensates for the excess slot inductance to provide the desired impedance for matching the antenna. However, when the feed line is terminated by an IDC, the stub length needs to be reduced to account for the larger capacitance provided by the IDC. Hence, in the second stage of the design, the IDC is placed at the end of the feedline, and its geometry, position, as well as the slot length are optimized in full-wave EM simulation (using CST Studio Suite [37]) to produce resonance at 2.45 GHz. This also required the patch length to be adjusted slightly to tune the resonance to the desired frequency. The final dimensions of the IDC, patch and the feed line are listed in Table 1. Fig. 2 displays the overall size of the IDC. The feed line length includes the stub. The slot aperture length is a critical parameter which determines the extent of coupling between the feed line and the patch. For higher isolation between the IDC sensor and the patch antenna, less than critical coupling is highly desirable. To prevent over coupling, the slot length must be made no larger than required. A narrow slot width is chosen to make the

electric field uniform within the coupling region.

Next, we present important simulated results of the SACP antenna. The simulated return loss of the optimized SACP antenna (without material loading of the IDC) is depicted in Fig. 3, reaching its maximum (54.65 dB) at 2.453 GHz with an input impedance of  $49.9 \Omega$ . For comparison, the return loss of the measured SACP antenna is also plotted, showing excellent agreement with the simulated result. The reader is referred to [35] for a discussion on the simulated radiation pattern. To summarize, the simulated realized gain is 6.35 dBi, the radiation efficiency is -0.77 dB, and the side lobe levels in the two principal planes are -18 dB.

TABLE I  
OPTIMIZED SACP ANTENNA DIMENSIONS

Parameter	Dimension (mm)
Substrate width / length	75 / 80
Rectangular patch width / length	30 / 41
Microstrip line width / length	3.3 / 40
IDC finger width / length	1 / 11.5
IDC finger pitch	0.5
Aperture width / length	1.5 / 12.4

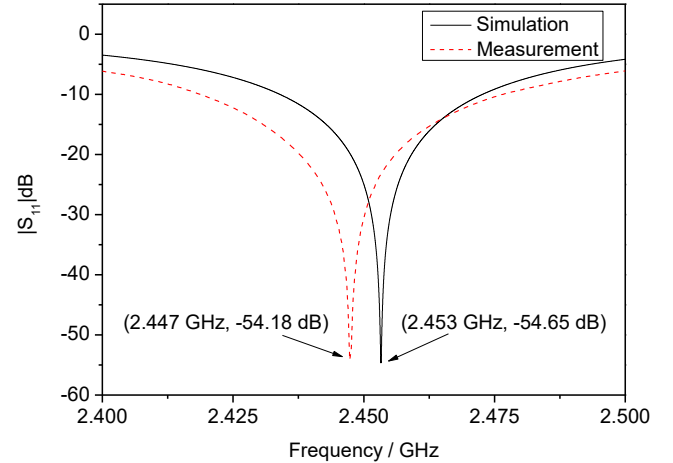


Fig. 3. S11 magnitude. Simulation and measurement of the resonance at 2.45 GHz.

Fig. 4 shows a plot of the electric field intensity on the surfaces of the patch, the feed line and the IDC at the resonant frequency of 2.45 GHz. The feed line is oriented along the  $y$ -direction, the slot length is along the  $x$ -direction, and the patch length is along the  $y$ -direction. The dominant mode is evident on the surface of the patch with a sinusoidal distribution along the patch length, reaching its maximum at the edges and a null at the center. The field distribution over the IDC surface is weak (ten orders of magnitude smaller than the maximum electric field on the patch), signifying the lack of electromagnetic interference between the sensor and the antenna. This is clear evidence of the fact that the antenna performance is not affected by the sensor and vice versa.

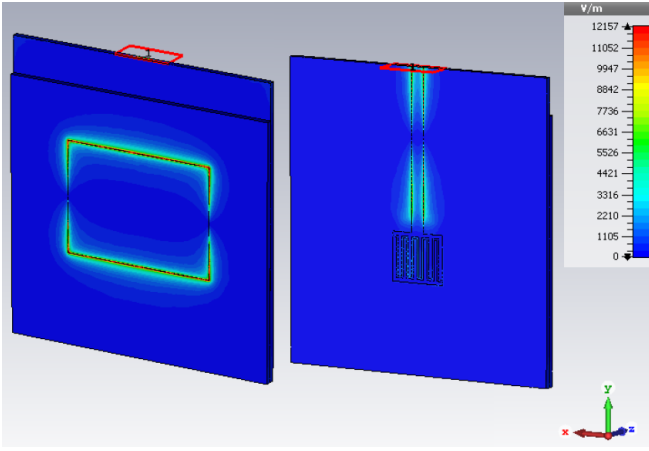


Fig. 4. The simulated electric field distribution on the SACP antenna (left) and the IDC sensor element (right).

### III. EXPERIMENTAL DETAILS

#### A. Antenna Fabrication and Characterization

After its design and optimization, the SACP antenna was fabricated on Rogers RO4003C substrate using the LPKF Protomat S103 PCB Milling Machine. An SMA connector was soldered at the end of the microstrip line creating the excitation port. A plastic frame was also fabricated with a 3D printer for the ACP assembly [35]. The antenna and the sensor boards were fabricated separately with two independent ground planes and centered slots. The frame design allows to move one substrate with respect to the other in  $x$  and  $y$  directions for precise alignment of the two slots. If the two apertures in the ground planes are not well-aligned, the antenna performance is compromised. The simulations reveal that the return loss is strongly influenced by the alignment of the boards (i.e. aperture size and position), while the resonant frequency is affected by the dimensions of the rectangular patch. The fabricated antenna and its plastic alignment frame are shown in Fig. 5.

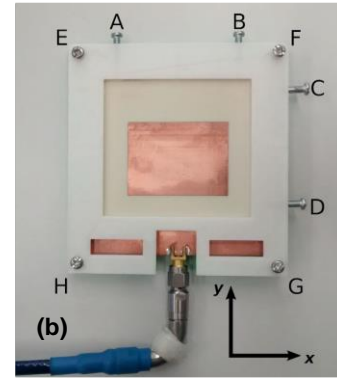
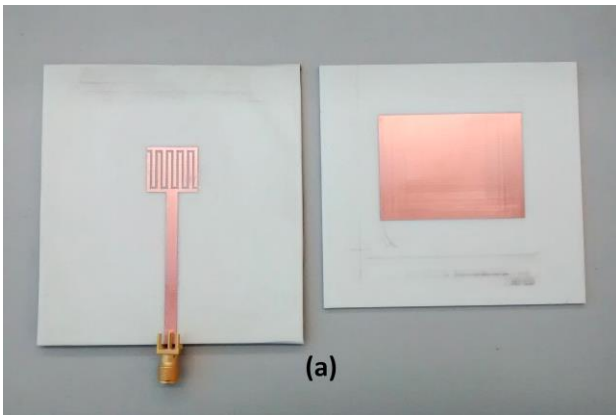


Fig. 5. (a) Realized SACP antenna with the IDC-loaded feed line (left) and the patch resonator (right) on two separate substrates. (b) The 3D printed plastic frame to align the antenna and the feed substrates. Screws A and B move the antenna substrate in the vertical direction. Screws C and D move the antenna in the horizontal direction. Screws E, F, G and H lock the substrate in the optimized position.

Microwave measurements on the fabricated antenna are carried out using Rohde & Schwarz ZNB20 Vector Network Analyzer (VNA). As shown in Fig. 3, the measured return loss of the SACP antenna at resonance (2.447 GHz) is 54.18 dB. Interestingly, the simulated and measured resonant frequencies deviate only 3 MHz (or 0.01%) on either side of the design value of 2.45 GHz. This small difference in the resonant frequency is attributed to dimensional tolerances of the fabricated antenna.

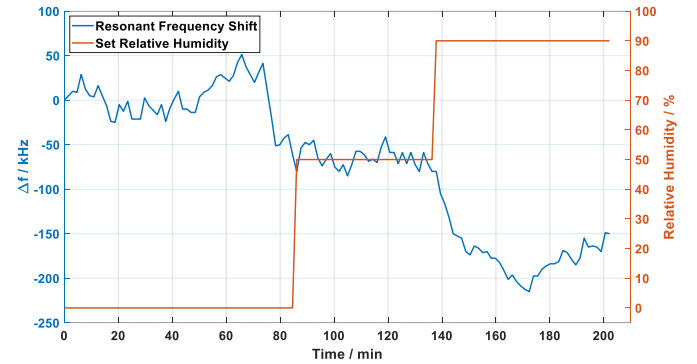


Fig. 6. Frequency shift at different humidity concentrations relative to the resonant frequency in dry air (10 %RH). All measurements are conducted at room temperature ( $24\text{ }^{\circ}\text{C} \pm 1\text{ }^{\circ}\text{C}$ ).

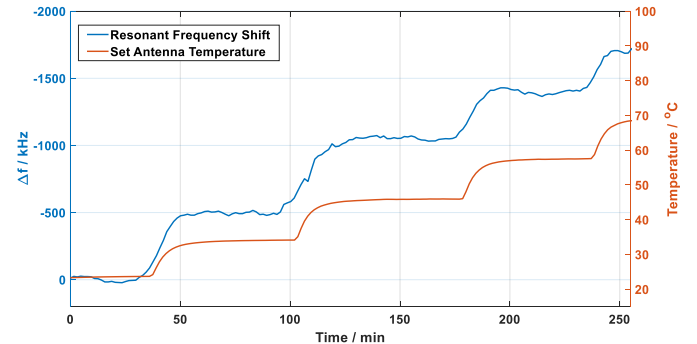


Fig. 7. Resonant frequency shift for a constant humidity (10%) at different



antenna temperatures, relative to the resonant frequency at 24 °C.

The main goal of this research is the development of a humidity sensor integrated into a 2.45 GHz ACP antenna. Temperature and humidity play a significant role in the response of gas sensors. Therefore, before deposition of the sensing material, the ACP antenna sensor is characterized in terms of its *baseline* response to temperature and humidity variation. According to these measurements, while the resonant frequency of the antenna is relatively insensitive to humidity variation (2 kHz per %RH – see Fig. 6), it has higher variation with temperature at 32 kHz/°C (see Fig. 7). This is reasonable because of the thermal expansion of the substrate (11, 14, 46 ppm/°C in *x*, *y*, *z* directions, respectively) [38], [39], and the thermal coefficient of the dielectric constant (40 ppm/°C) [39].

### B. Sensing Material Synthesis and Deposition

After the antenna fabrication, the sensing material is deposited on the surface of the IDC. Nano-powder of barium titanate oxalate with urea coating ( $\text{BaTiO}(\text{C}_2\text{O}_4)_2/\text{CO}(\text{NH}_2)_2$ ) is selected for this project. Its synthesis is similar to that reported in [40], [41]. The main pathway steps are summarized in Fig. 8. Barium chloride ( $\text{BaCl}_2$ ) was added to 300 ml of water at a temperature of 60 °C. The compound was mixed for few minutes in order to stabilize the  $\text{BaCl}_2$  (solution A). Another solution was prepared starting from 300 ml of water at 60 °C and mixing it with oxalic acid ( $\text{H}_2\text{C}_2\text{O}_4$ ). After the solubilization, the titanium tetrachloride ( $\text{TiCl}_4$ ) was added (solution B). Solutions A and B were then mixed for one hour at 60 °C, leading to the formation of intermediate barium titanate oxalate ( $\text{BaTiO}(\text{C}_2\text{O}_4)_2$ ). This intermediate product formed was then filtered, washed with water and placed inside an oven at 80 °C for 12 hours. The dried precipitate was dispersed in a solution of urea (with a ratio of 1:3) and the mixture was stirred for 30 minutes. Finally, the formed  $\text{BaTiO}(\text{C}_2\text{O}_4)_2/\text{CO}(\text{NH}_2)_2$  composite product was filtered, washed and dried in oven for 12 hours at 80 °C.

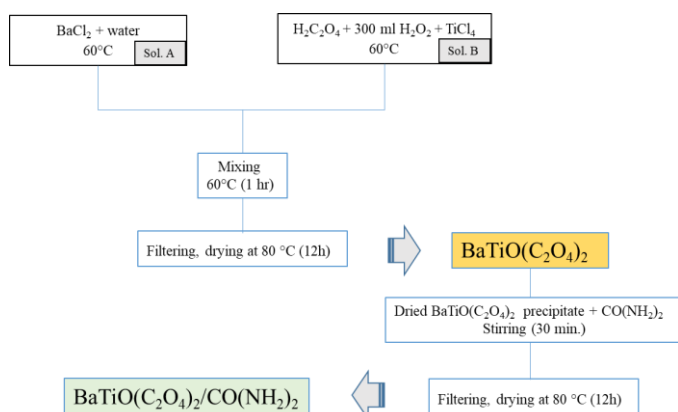


Fig. 8. Flowchart of the synthesis of the  $\text{BaTiO}(\text{C}_2\text{O}_4)_2/\text{CO}(\text{NH}_2)_2$ .

SEM (Scanning Electron Microscopy) analysis of  $\text{BaTiO}(\text{C}_2\text{O}_4)_2/\text{CO}(\text{NH}_2)_2$  composite highlighted the presence of agglomerates of nanoparticles with bundle size less than 5  $\mu\text{m}$  (Fig. 9a). These agglomerates have a spherical shape and appear to consist of primary grains of nanometric size.

Subsequently, TEM (Transmission Electron Microscopy) analysis proved that each grain is characterized by an inner crystalline core made of  $\text{BaTiO}(\text{C}_2\text{O}_4)_2$  and an external amorphous coating of urea (see yellow arrows) with a thickness of 3-5 nm (Fig. 9b).

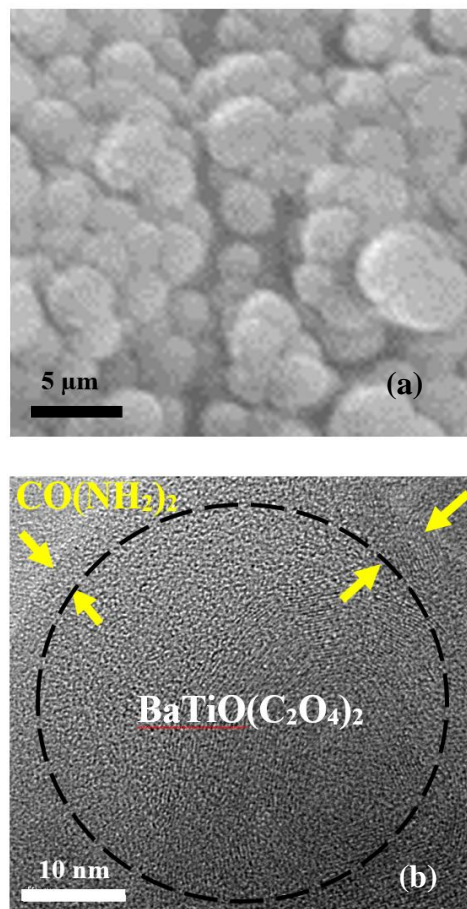


Fig. 9. SEM (a) and TEM (b) analysis of the  $\text{BaTiO}(\text{C}_2\text{O}_4)_2/\text{CO}(\text{NH}_2)_2$  nanoparticles.

In order to confirm the observations made, a microstructural characterization has been carried out by XRD and FT-IR analysis. The XRD spectrum (Fig. 10) in the wide 2-theta range shows the presence of a multitude of diffraction peaks, assigned to the crystalline phase  $\text{BaTiO}(\text{C}_2\text{O}_4)_2$ . In the inset, is shown a limited region of the 2-theta range, which evidences better the individual diffraction peaks, thus confirming the good crystallinity of the synthesized material.

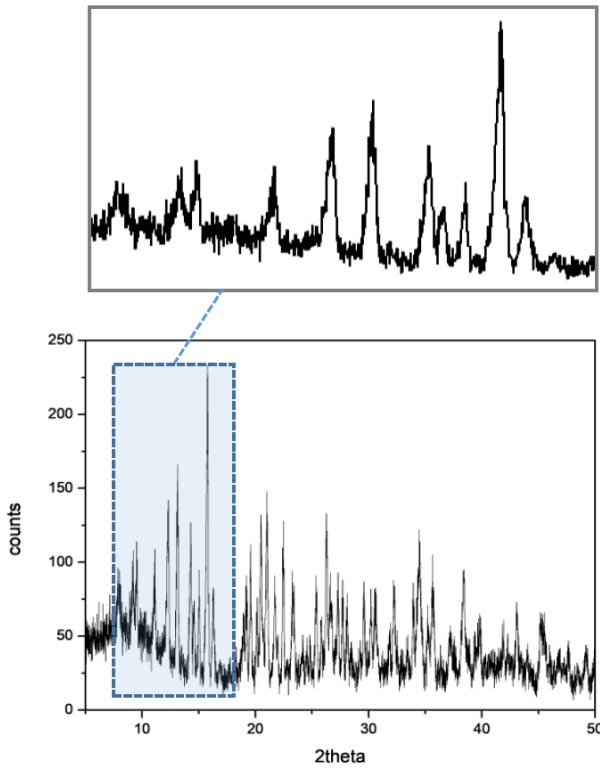


Fig. 10. XRD spectrum of the urea coated  $\text{BaTiO}_3$  sample.

The FT-IR analysis (see Fig. 11) of  $\text{BaTiO}(\text{C}_2\text{O}_4)_2/\text{CO}(\text{NH}_2)_2$  highlighted the presence of typical peaks characterizing  $\text{BaTiO}(\text{C}_2\text{O}_4)_2$ . The band at  $3450\text{ cm}^{-1}$  is due to stretching of the adsorbed water. The band at  $1692\text{ cm}^{-1}$  is related to the hydroxyl group absorption. The bands corresponding to the symmetrical stretching of C-O and C-C groups are centered at  $1491\text{ cm}^{-1}$  and  $1273\text{ cm}^{-1}$ , respectively. The peak at  $815\text{ cm}^{-1}$  is due to the stretching of Ti-OH. Finally, the adsorption dips at  $3412\text{ cm}^{-1}$  and  $1623\text{ cm}^{-1}$  characterize the N-H bond due to the presence of the urea coating, which proves the composite composition as  $\text{BaTiO}(\text{C}_2\text{O}_4)_2/\text{CO}(\text{NH}_2)_2$ .

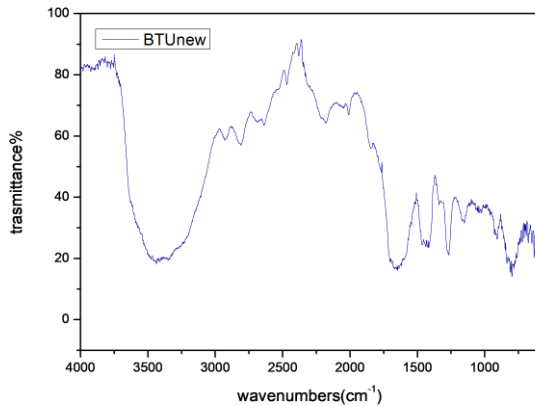


Fig. 11. FT-IR spectrum of the  $\text{BaTiO}(\text{C}_2\text{O}_4)_2/\text{CO}(\text{NH}_2)_2$  composite sample.

#### IV. SENSOR PERFORMANCE

The material thus produced looks like white powder. It was mixed with water and deposited on the IDC fingers using the drop-coating technique. At the end of the process, the material in excess was removed so that only the material between the fingers remained (with a thickness of  $17\text{ }\mu\text{m}$ ). Further tests on the antenna proved that the sensing material deposition reduced the resonant frequency by only  $62.5\text{ kHz}$  and the return loss by  $3.6\text{ dB}$ . After the material deposition, the sensing performance is tested at different humidity concentrations and temperatures. The SACP antenna with its plastic frame is placed inside the humidity generator, Thunder Scientific 2500, close to the glass window in order to avoid the EM reflected waves off the metallic walls. First, the temperature inside the chamber is maintained constant at  $23\text{ }^\circ\text{C}$  and the sensor is exposed to four different levels in humidity (10% (dry air), 40%, 80%, 95% RH). The scattering parameter  $S_{11}$  is measured every minute in order to extract the resonant frequency shift relative to the baseline frequency corresponding to the average of the initial 10% RH data. At the end of each humidity exposure cycle, the humidity is set to 10% RH in order to allow the sensor to return to its baseline. No significant frequency shifts are observed for relative humidity lower than 40% (see Fig. 12). On the contrary, at higher humidity levels the antenna resonant frequency changes with the humidity concentration. For a variation from 10% RH to 95% RH a shift of approximately  $600\text{ kHz}$  is recorded. It is worth noting that the sensor returns to its baseline at the end of each humidity step. Next, the same measurements are performed at  $30\text{ }^\circ\text{C}$  with different results, as depicted in Fig. 13. In fact, at the higher temperature, for the same relative humidity concentration, the water content in the air is higher. This explains why at this temperature the sensitivity is also higher, with an observed frequency shift of  $1.2\text{ MHz}$  for the same 10% RH to 95% RH humidity variation. Even in this case, no significant frequency shifts were observed for humidity levels lower than 40% RH. The measurements are repeated at  $40\text{ }^\circ\text{C}$ , and similar conclusions have been observed (results not plotted for brevity). These results confirm that nanomaterial loading does not impact the performance of either the antenna or the sensor due to weak coupling between the two.

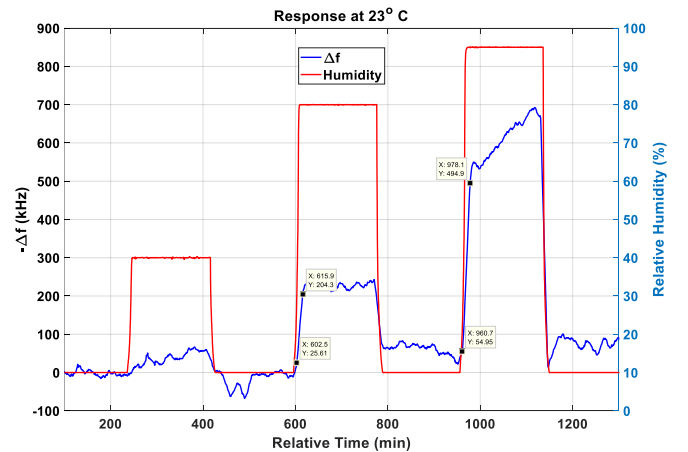


Fig. 12. Antenna resonant frequency shift at different relative humidity concentrations ( $T = 23\text{ }^\circ\text{C}$ ).

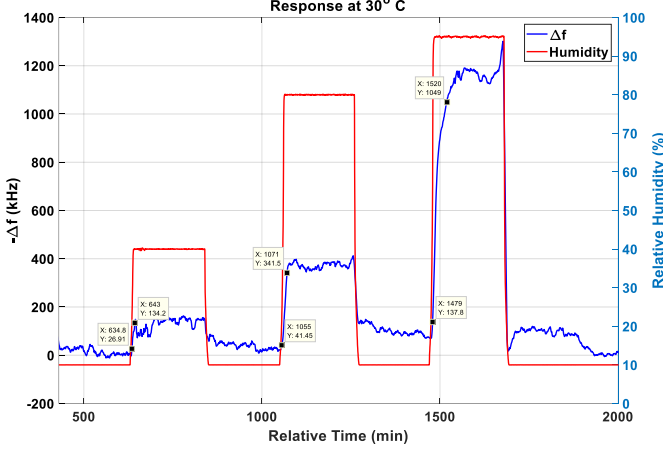


Fig. 13. Antenna resonant frequency shift at different relative humidity concentrations ( $T = 30^\circ\text{C}$ ).

It is worth comparing the humidity response measurements of the SACP antenna before and after the sensing material deposition in order to determine the improvement in sensitivity. In the former case, at room temperature, a frequency shift of 200 kHz was recorded for humidity variation from dry air to 90 % RH (see Fig. 6), with sensitivity of 2 kHz per %RH. In the latter case (Fig. 12), a shift of 600 kHz is observed for humidity variation from dry air to 95 % RH, yielding sensitivity of 6.3 kHz per %RH. This vast improvement (215%) in sensitivity to humidity validates the superior sensing performance of barium titanate deposited between the IDC fingers. At higher temperatures, the sensitivity improves further as indicated in Fig. 13.

#### A. Baseline Drift

It is observed from Figs. 12 and 13 that the sensor retracts to the baseline satisfactorily once dry air is injected into the test chamber after cycling each humidity level. Due to hysteresis, measurement noise, and random errors inherent in the physical interaction processes occurring at the sensing film nanostructure, it is expected that there will be some baseline drift during each desorption cycle following the gas exposure. In order to quantify this drift, the sensor response at room temperature in dry air, measured in between the humidity adsorption cycles, is replotted in Fig. 14. For the four dry air cycles shown, the average frequency shifts are found to be 7.4032, -15.3204, 62.5736, and 77.7663 kHz. Thus, the drift increases during the desorption cycles following higher humidity level exposures. This is reasonable to expect because the rate of desorption in nanostructured gas sensors slows down with increasing gas concentration levels [11], [12]. At room temperature, the average drift over almost 24 hours is 33 kHz (mean of the four blue segments). This baseline drift is relatively small (only 5%) in comparison with the sensor response to variation in humidity from 10% RH to 95% RH, i.e., a frequency shift of 600 kHz (Fig. 12). As temperature increases, the baseline drift becomes even smaller in proportion

to the overall response swing (see Fig. 13). However, long-term exposure and desorption cycles need to be investigated to evaluate the impact of drift on the humidity sensor calibration.

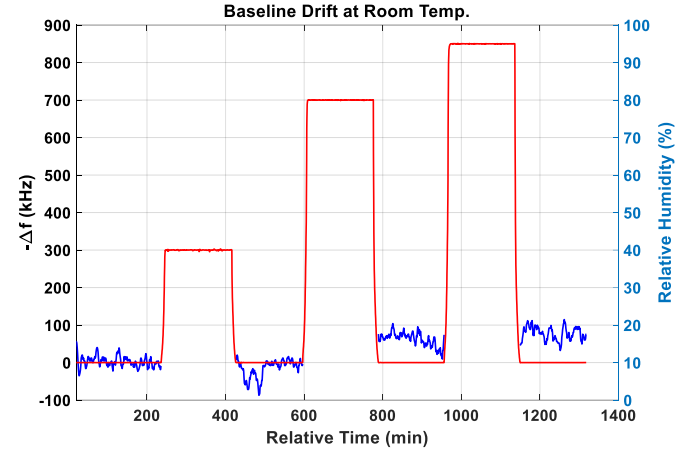


Fig. 14. Antenna resonant frequency shift during the desorption cycles characterized by dry air ( $T = 23^\circ\text{C}$ ). The blue line is the sensor response and the red line denotes the humidity profile.

#### B. Response Time

Table II displays the response times of the humidity sensor, calculated from the resonant frequency shifts at each temperature. For each humidity level, the response time is defined as the time taken by the sensor to respond between the limits corresponding to 10% and 90% of the steady state response [42]. These limits are denoted by markers on the graphs in Figs. 12 and 13. Table II also indicates the response time for the stimulus to reach the set humidity level from the baseline of 10% RH. It is observed that the sensor response tracks the stimulus change almost instantaneously. In general, the sensor reaches steady state (90% level) in less than a minute after the set humidity level is attained in the chamber. The only exception is the 30 °C case, which entails steady state response times of 2 min and 22 min for 80% RH and 95% RH, respectively. The 95% RH level overall response time of 41 min appears to be an outlier and is perhaps caused by random measurement errors. Overall, relative response times less than a minute seem to be the trend for the humidity response to reach steady state. The response times in Table II pertain to adsorption of water molecules by the sensor material. It is equally important to examine the desorption times indicating the time taken to desorb the water vapor and return to the baseline. From Figs. 12 and 13, it is evident that the desorption times, typically less than 30 s, are faster than the adsorption times. In comparison to metal oxide sensors which require heating up to 500 °C for desorption times less than a minute [2], [7], the proposed SACP antenna sensor can attain fast desorption without sensor heating. This is very attractive to its implementation in low-power wireless sensor networks as an IoT node for ambient humidity measurements.



TABLE II  
RESPONSE TIME OF THE SENSOR

Temperature (°C)	Relative Humidity (%)	Response Time (min)	
		Stimulus	Sensor
23	40	12.3	12.6
	80	13.0	13.4
	95	17.0	17.4
30	40	12.0	12.4
	80	14.1	16.0
	95	18.6	41.0
40	40	11.4	12.2
	80	13.0	13.2
	95	15.0	15.3

### C. Baseline Temperature Effects of the Sensing Material

Next, we investigate the baseline sensing performance in dry air as a function of temperature to determine the temperature effects of  $\text{BaTiO}(\text{C}_2\text{O}_4)_2/\text{CO}(\text{NH}_2)_2$  film deposition. Dry air is chosen to eliminate any confounding effects of humidity, which are discussed in Section IV D. Measurements were performed on the SACP antenna at different temperatures by placing it inside the MBW Thunder Scientific 2500 Climatic Chamber, close to the glass window. Its resonant frequency was monitored at six different temperatures spanning  $-10^\circ\text{C}$  to  $40^\circ\text{C}$  in steps of  $10^\circ\text{C}$ , at a relative humidity of 10% (dry air), using the Vector Network Analyzer. Choosing an arbitrary reference temperature as  $-10^\circ\text{C}$ , the relative resonance shift is plotted in Fig. 15. Using a linear fit to the average steady state response over each temperature cycle, a sensitivity of  $40 \text{ kHz}/^\circ\text{C}$  is estimated from the measurements recorded by the VNA. This value is close to that obtained in the baseline sensitivity of  $32 \text{ kHz}/^\circ\text{C}$  for the ACP antenna without the sensing material (see Fig. 7). This means that the sensing material does not appreciably change its permittivity with temperature, and the small increase in the observed frequency shift in Fig. 15 is due to thermal expansion of copper on the antenna surface and the temperature dependence of the antenna substrate.

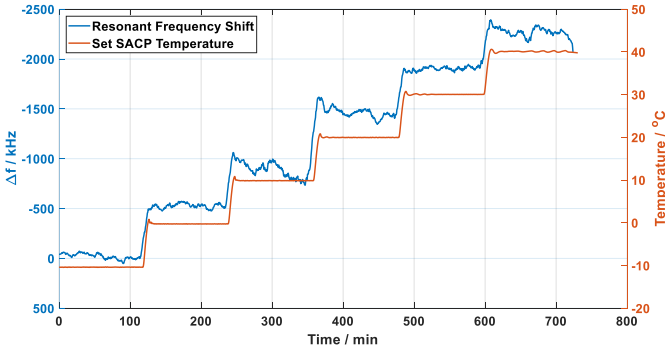


Fig. 15. Measured sensor-loaded antenna resonant frequency in response to temperature variation.

### D. Sensor Calibration

The SACP sensor response depends on both humidity and temperature as the former is affected by the latter. In this Section, this dependence is examined to determine any confounding effect of the temperature and the sensor calibration is discussed. For the sensor calibration, measurements have been carried out in the temperature range from  $10^\circ\text{C}$  to  $40^\circ\text{C}$  in four different steps. For each temperature the antenna performance has been tested considering the following relative humidity concentrations: 10%, 40%, 50%, 80%, 95%. For each set point at least 30 measurements have been acquired and the mean values have been taken into account for calibration. The standard deviation of each acquired dataset was less than 20 kHz. Fig. 16 plots all the temporal samples of the SACP measurements as a 3D graph depicting the simultaneous dependence of the resonant frequency shift (relative to baseline) on humidity (RH) and temperature (T) within the range  $10\% \leq \text{RH} \leq 95\%$  and  $10 \leq T \leq 40^\circ\text{C}$ . The response surface given by

$$\Delta f = a \exp\left(b/RH + c/(d + eT + gT^2)\right) \quad (1)$$

is fit to the frequency shift with RMS error of 22 kHz and  $R^2 = 0.99$ , where the model coefficients are  $a = -3959$ ,  $b = -665.3$ ,  $c = 3774$ ,  $d = -3796$ ,  $e = 247.5$  and  $g = -7.461$ . The residuals appear randomly scattered around zero indicating that the model describes the data well. The response surface is relatively flat for  $\text{RH} < 50\%$  and varies exponentially with humidity at higher levels. Higher humidity and temperature levels are associated with a larger slope of the response surface, presumably due to higher rate of evaporation with increasing temperature. Interestingly, the measured data for a given temperature and humidity clusters around its mean, indicating that the measurements are reasonably well-controlled and majority of the observed variation is caused by the sensor. It may be surmised that temperature confounding is a factor only at the higher humidity levels.

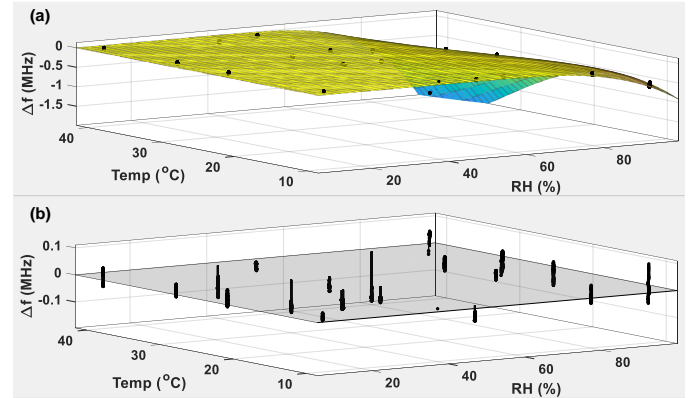


Fig. 16. (a) Response surface of the measured sensor data as a function of humidity and temperature. (b) Residuals.

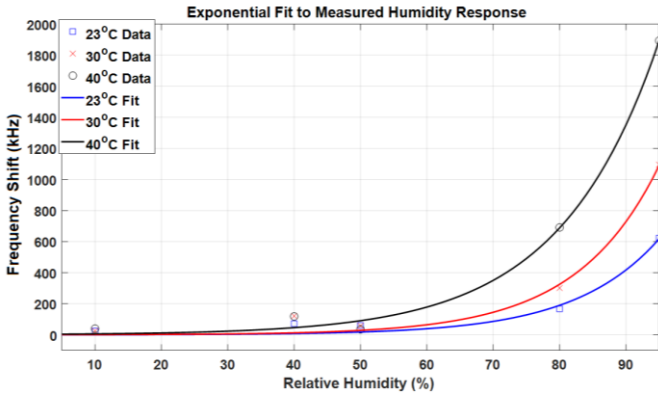


Fig. 17. Humidity response calibration curves at selected temperatures.

By considering the steady state sensor response as a function of humidity, the sensor calibration can be investigated. Fig. 17 displays the sensor calibration curves at various temperatures. At each temperature, the humidity response is fit to an exponential curve given by  $-\Delta f = a_1 \exp(b_1/RH)$ . It is reaffirmed that  $RH > 40\%$  yields faster exponential growth and the sensor response is relatively flat for the lower humidity levels, which is in agreement with prior investigations on nanotechnology-based conductimetric [43] and capacitive [44], [45] humidity sensors. The sensitivity at each temperature is calculated from the slope of the exponential calibration curve, and plotted in Fig. 18. Because of goodness of the fit to the measured data, the estimated sensitivity will be close to the sensitivity computed using the measured data points. It is evident that sensitivity also increases exponentially with humidity as well as temperature.

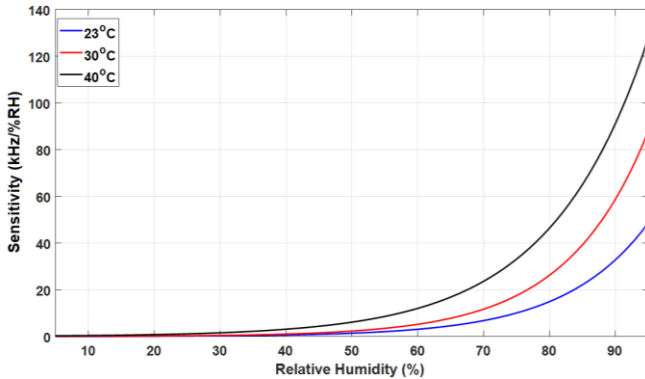


Fig. 18. Sensitivity of the humidity response at selected temperatures.

## V. CONCLUSION

In this paper, we have reported on the design, fabrication and testing of a printed sensor integrated into a 2.45 GHz ACP antenna. The sensing element consists of a printed interdigitated capacitor (IDC) covered by a nanostructured material based on barium titanate. The IDC is located at the end of the microstrip line feeding the ACP antenna. The positioning of the IDC at the open end of the line and the aperture coupling through a slot separating the two substrates helps ensure that the coupling

between the sensor and the patch antenna is minimized, a necessary condition for improved sensitivity. This allows one to overcome the detuning issues and the loss in sensitivity affecting the classical configuration of direct line-fed patch antenna sensor [19].

The SEM/TEM analysis of a  $\text{BaTiO}(\text{C}_2\text{O}_4)_2/\text{CO}(\text{NH}_2)_2$  sample highlighted the presence of uniform spherical agglomerates (with size less than  $5 \mu\text{m}$ ) comprising primary crystals with nanometric size (3-5 nm). The performance of the sensor-integrated ACP antenna to relative humidity and temperature variations has been investigated experimentally after deposition of the sensing material. The fact that resonance shifts of the order of few hundred kHz to approximately 2 MHz have been measured by the SACP antenna for humidity and temperature within the range  $10\% \leq RH \leq 95\%$  and  $10 \leq T \leq 40$  ( $^\circ\text{C}$ ), respectively, without detuning the center frequency, proves that minimum coupling between the sensing element and the antenna has been achieved. *This is the first successful design of an SACP antenna, demonstrated herein for humidity detection, but it holds promise in general as a nanotechnology-based gas sensor element in wireless sensing nodes (such as IoT).* For IoT applications in the 2.45 GHz ISM band, the proposed sensor design is relatively immune to ambient EMI because the antenna and the sensor are strongly decoupled as shown by the measurements.

A comparison of the humidity response measurements before and after the sensing material deposition reveals the improvement in sensitivity of this novel design. In the former case, at room temperature, a frequency shift of 200 kHz was recorded for humidity variation from dry air to 90 %RH, with sensitivity of 2 kHz per %RH. In the latter case, a shift of 600 kHz is observed for humidity variation from dry air to 95 %RH, yielding sensitivity of 6.3 kHz per %RH. This vast improvement (215%) in sensitivity to humidity validates the superior sensing performance of  $\text{BaTiO}(\text{C}_2\text{O}_4)_2/\text{CO}(\text{NH}_2)_2$  deposited between the IDC fingers. At higher temperatures, the sensitivity improves further. The sensor calibration follows an exponential behavior, indicating higher sensitivities at high RH levels and flattening out at the lower levels.

## REFERENCES

- [1] "Global sensor market forecast 2022: IoT and wearables as drivers", [www.i-scoop.eu/global-sensor-market-forecast-2022/](http://www.i-scoop.eu/global-sensor-market-forecast-2022/)
- [2] G. F. Fine, L. M. Cavanagh, A. Afonja, and R. Binions, "Metal Oxide Semi-Conductor Gas Sensors in Environmental Monitoring," *Sensors* 2010, 10, 5469-5502; doi:10.3390/s100605469.
- [3] K. Narimani, F. D. Nayeri, M. Kolahdouz, and P. Ebrahimi, "Fabrication, modeling and simulation of high sensitivity capacitive humidity sensors based on ZnO nanorods," *Sensor. Actuat. B Chem.* 224 (2016) 338-343.
- [4] L. Rassaei, F. Marken, M. Sillanpää, M. Amiri, C. MihaiCirtiu, and M. Sillanpää, "Nanoparticles in electrochemical sensors for environmental monitoring," *TrAC Trends in Analytical Chemistry*, Vol. 30, Issue 11, pp. 1704-1715, Dec 2011.
- [5] S. J. Patil, A. Adhikari, M. S. Baghini, and V. R. Rao, "An ultra-sensitive piezoresistive polymer nano-composite microcantilever platform for humidity and soil moisture detection," *Sensor. Actuat. B-Chem.* 203 (2014) 165-173.
- [6] MacDonnell, M., M. Raymond, D. Wyker, M. Finster, Y. Chang, T. Raymond, B. Temple, M. Scofield, D. Vallano, E. Snyder, AND R. Williams. *Mobile Sensors and Applications for Air Pollutants*. U.S.

- Environmental Protection Agency, Washington, DC, EPA/600/R-14/051 (NTIS PB2014 105955), 2014.
- [7] René Lalauze (Ed.), *Chemical Sensors and Biosensors*, Wiley Online Library, DOI: 10.1002/9781118561799, 2013.
  - [8] Y. Liu, H. Huang, L. Wang, D. Cai, B. Liu, D. Wang, et al., "Electrospun CeO<sub>2</sub> nanoparticles/PVP nanofibers based high-frequency surface acoustic wave humidity sensor," *Sensor. Actuat. B-Chem.* 223 (2016) 730-737.
  - [9] M.-I. Baraton and L. Merhari, "Advances in air quality monitoring via nanotechnology," *Journal of Nanoparticle Research*, vol. 6: 107-117, 2004.
  - [10] Bekyarova, E.; Kalinina, I.; Itkis, M. E.; Beer, L.; Cabrera, N.; Haddon, R. C., "Mechanism of ammonia detection by chemically functionalized single-walled carbon nanotubes: In situ electrical and optical study of gas analyte detection," *J. Am. Chem. Soc.* 2007, 129, 10700-10706.
  - [11] Colindres, S. C.; Aguir, K.; Sodi, F. C.; Vargas, L. V.; Salazar, J. A. M.; Febles, V. G., "Ozone Sensing Based on Palladium Decorated Carbon Nanotubes," *Sensors* 2014, 14, 6806-6818.
  - [12] D. Ziegler, E. Bekyarova, A. Marchisio, J.-M. Tulliani, and K. Naishadham, "Highly Selective Ozone Sensors Based on Functionalized Carbon Nanotubes," *IEEE Sensors Conference*, New Delhi, Oct. 2018.
  - [13] S. Chopra, A. Pham, J. Gaillard, A. Parker, and A. M. Rao, "Carbon-nanotube-based resonant circuit sensor for ammonia," *Appl. Phys. Lett.*, vol. 80, no. 24, pp. 4632-4634, June 2002.
  - [14] K. Chang, Y. H. Kim, Y. J. Kim, and Y. J. Yoon, "Functional antenna integrated with relative humidity sensor using synthesized polyimide for passive RFID sensing," *Electron Lett.*, vol. 43, no. 3, pp. 7-8, 2007.
  - [15] G. Barochi, J. Rossignol, and M. Bouvet, "Development of microwave gas sensors," *Sensors Actuators B-Chem.*, vol. 157, no. 2, pp. 374-379, Oct. 2011.
  - [16] M. Dragoman, D. Neculoiu, A. Cismaru, A. A. Muller, G. Deligeorgis, G. Konstantinidis, D. Dragoman, and R. Plana, "Coplanar waveguide on graphene in the range 40 MHz-110 GHz," *Appl. Phys. Lett.* 99, 033112, 2011.
  - [17] L. Yang, R. Zhang, D. Staiculescu, C.P. Wong, M.M. Tentzeris, "A novel conformal RFID-enabled module utilizing inkjet-printed antennas and carbon nanotubes for gas detection applications," *IEEE Antennas Wireless Propagat. Lett.*, Vol. 8, pp. 653-656, 2009.
  - [18] H. Lee, K. Naishadham, M. M. Tentzeris, and G. Shaker, "A novel highly-sensitive antenna-based gas sensor utilizing carbon nanotubes and inkjet printing," *IEEE Antennas Propagat. Symp.*, Spokane, USA, July 2011.
  - [19] H. Lee, G. Shaker, K. Naishadham, X. Song, M. McKinley, B. Wagner, and M. M. Tentzeris, "Carbon nanotube loaded antenna-based ammonia gas sensor," *IEEE Trans. Microwave Theory Tech.*, vol. 59, no. 10, pp. 2665-2673, Oct. 2011.
  - [20] K. Naishadham, E. Bekyarova, and P. Savi, "Passive Nanotechnology Based Sensors for the Remote Detection of Environmental Pollutants Impacting Public Health," *IEEE Sensors Conference*, Glasgow, Scotland, Oct. 2017.
  - [21] G. Gugliandolo, A. Mirzaei, M. Bonyani, G. Neri, M. Latino, and N. Donato, "Electrical Characterization of Microstrip Resonators Based on Nanostructured Sensing Materials", *Lecture Notes in Electrical Engineering*, 457, pp. 29-34, 2018.
  - [22] H. El Matbouly, N. Boubekeur, and F. Domingue, "Passive microwave substrate integrated cavity resonator for humidity sensing," *IEEE Trans. Microwave Theory and Tech.* vol. 36, pp. 4150-4156, Dec. 2015.
  - [23] M. Ndoye, I. Kerroum, D. Deslandes, and F. Domingue, "Air-filled substrate integrated cavity resonator for humidity sensing," *Sensor. Actuat. B-Chem.* 252 (2017) 951-955.
  - [24] T. G. Kang, J. K. Park, G. H. Yun, H. H. Choi, H. J. Lee, and J. G. Yook, "A real-time humidity sensor based on a microwave oscillator with conducting polymer PEDOT: PSS film," *Sensor. Actuat. B-Chem.* 282 (2019) 145-151.
  - [25] J. K. Park, T. G. Kang, B. H. Kim, H. J. Lee, H. H. Choi, J. G. Yook, "Real-time humidity sensor based on microwave resonator coupled with PEDOT: PSS conducting polymer film," *Sci. Rep.* 8 (2018) 493.
  - [26] Cándid Reig and Ernesto Ávila-Navarro, "Printed Antennas for Sensor Applications: A Review," *IEEE Sensors J.*, Vol. 14, No. 8, pp. 2406-2418, Aug. 2014.
  - [27] D. M. Pozar, "Microstrip antenna aperture-coupled to a microstripline", *Electronics Letters*, vol. 21, no. 2, pp. 49-50, Jan. 17, 1985.
  - [28] D. M. Pozar, "A Review of Aperture Coupled Microstrip Antennas: History, Operation, Development, and Applications," Technical Report, (<http://www.ecs.umass.edu/ece/pozar/aperture.pdf>), May 1999.
  - [29] T. Milligan, *Modern Antenna Design*. New York: McGraw-Hill, 1985.
  - [30] D. M. Pozar and S.H. Schaubert (Eds.), *The Analysis and Design of Microstrip Antennas and Arrays*, Piscataway, NJ: IEEE Press, 1995.
  - [31] R. Garg, *Microstrip Antenna Design Handbook*, Norwood, MA: Artech House, 2001.
  - [32] R. B. Waterhouse, *Microstrip Patch Antennas: A Designer's Guide*, Kluwer Academic Publishers, 2003.
  - [33] K. Naishadham, "Design of a graphene loaded slot antenna with 100:1 bandwidth for wireless sensor applications," *IEEE Antennas and Propagation Soc. Int. Symposium*, Memphis, TN, 2014.
  - [34] K. Naishadham, "Design of a compact wideband slot antenna using parasitic reactive tuning," 44<sup>th</sup> European Microwave Conf., Rome, Italy, 2014.
  - [35] G. Gugliandolo, K. Naishadham, N. Donato, G. Neri, and V. Fericola, "Sensor-Integrated Aperture Coupled Patch Antenna," *IEEE International Symposium on Measurements & Networking (M&N)*, Catania, Italy, July 2019.
  - [36] M. M. Ahmed, K. Bhowmlk, A. Al Suman, "Analysis and Design of Rectangular Microstrip Patch Antenna on Different Resonant Frequencies for Pervasive Wireless Communication", *International Journal of Scientific & Technology Research*, vol. 1, no. 5, June 2012.
  - [37] CST Studio Suite, [https://www.3ds.com/products-services/simulia/products/cst-studio-suite/?utm\\_source=cst.com&utm\\_medium=301&utm\\_campaign=cst](https://www.3ds.com/products-services/simulia/products/cst-studio-suite/?utm_source=cst.com&utm_medium=301&utm_campaign=cst).
  - [38] J. W. Sanders, J. Yao, and H. Huand, "Microstrip patch antenna temperature sensor" *IEEE Sensors Journal*, vol. 15, no. 9, pp. 5312-5319, September 2015.
  - [39] Rogers Corporation, RO4000 Series High Frequency Circuit Materials, Data Sheet ([www.rogerscorp.com/documents/726/acs/RO4000-Laminates-RO4350BData-Sheet.pdf](http://www.rogerscorp.com/documents/726/acs/RO4000-Laminates-RO4350BData-Sheet.pdf))
  - [40] Zhang Xu-ping, Xu Ling-li, Wang Qing-liang, "Electro-rheological effect of barium titanate particles coated with urea and suspended in methyl silicone oil," *China Journal of China University of Mining and Technology* 17, 2007, 578-581.
  - [41] Weijia Wen, Xianxiang Huang, Shihe Yang, Kunquan Lu And Ping Sheng, "The giant electrorheological effect in suspensions of nanoparticles," *Nature Materials* 2, 2003, 727-730.
  - [42] A. Vergara, S. Vembu, T. Ayhan, M. A. Ryan, M. L. Homer, and R. Huerta, "Chemical gas sensor drift compensation using classifier ensembles," *Sensors and Actuators B: Chemical* 166 (2012) 320-329.
  - [43] M. Sasmal, T. K. Maiti, and T. K. Bhattacharyya, "Synthesis of Bovine Serum Albumin Conjugated With ZnO Nanosphere for High-Speed Humidity Sensing Application," *IEEE Sensors Journal*, vol. 16, no. 6, pp. 1510-1517, March 15, 2016, doi: 10.1109/JSEN.2015.2503363.
  - [44] M. I. Azmer, Q. Zafar, Z. Ahmad, and K. Sulaiman, "Humidity sensor based on electrospun MEH-PPV:PVP microstructured composite," *RSC Adv.*, 2016, 6, 35387-35393.
  - [45] A. Tripathy, S. Pramanik, A. Manna, S. Bhuyan, N. F. Azrin Shah, Z. Radzi, and N. A. Abu Osman, "Design and Development for Capacitive Humidity Sensor Applications of Lead-Free Ca,Mg,Fe,Ti-Oxides-Based Electro-Ceramics with Improved Sensing Properties via Physisorption," *Sensors* 2016, 16, 1135; doi:10.3390/s16071135.